Applied Materials Today 42 (2025) 102592

Contents lists available at ScienceDirect

Applied Materials Today

journal homepage: www.elsevier.com/locate/apmt

Modulated photoresponse in a naturally-occurring two-dimensional material

Aura Garcia [a], Raul D. Rodriguez [a,*], Tuan-Hoang Tran [a], Dmitry Cheshev [a], Nelson E. Villa [a], Daria Gorbunova [a], Lyubov Krasnoshchekova [a], Hao Liu [b], Bin Yang [b], Xin Jia [b], Qiang Ma [c], Tao Zhang [c], Jin-Ju Chen [d], Evgeniya Sheremet [a]

[a] Tomsk Polytechnic University, Lenina avenue, 30, 634050, Tomsk, Russia
[b] School of Chemistry and Chemical Engineering/State Key Laboratory Incubation Base for Green Processing of Chemical Engineering, Shihezi University, Shihezi, 832003, China
[c] Key Laboratory of Marine Materials and Related Technologies, Ningbo Institute of Materials Technology and Engineering, Chinese Academy of Sciences, Ningbo, 315201, China
[d] School of Materials and Energy, University of Electronic Science and Technology of China, Chengdu, 610054, China

ARTICLE INFO

Keywords:
Arsenic trisulfide (As_2S_3)
photoresponse
2D materials
2D semiconductors
self-trapped excitons

ABSTRACT

Engineering light-matter interactions in nanoscale systems is crucial for optoelectronics. In this context, we discovered a remarkable photoresponse effect in a few-layer arsenic trisulfide (As_2S_3), a naturally occurring van der Waals semiconductor. Our results evidence an exceptional photoresponse in As_2S_3, with surface potential changes of up to 80 mV under low-intensity white light illumination due to the formation of self-trapped excitons that generate localized dipoles. This mechanism enables the efficient modulation of 2D As_2S_3's surface potential without inducing free charge carriers, highlighting its potential as a photoresponsive material. We exploited this distinctive photoresponse to enhance the photocatalytic conversion of 4-nitrobenzenethiol to 4,4′-dimercaptoazobenzene by silver nanowires (AgNWs) deposited on the 2D material. The localized light-induced dipoles at the 2D material interface enhanced the plasmonic photocatalytic efficiency of AgNWs by 71 %. The ability to photo-modulate collective electron oscillations and charge transfer in AgNWs indicates that As_2S_3 is a promising 2D material for optoelectronic applications, including photoswitches, photoelectric devices, and photovoltaic systems.

1. Introduction

The demand for increasingly efficient and miniaturized technologies has intensified the search for nanoscale materials with performance surpassing the current state-of-the-art. These materials must not only exhibit superior performance but also be readily available, cost-effective, and easy to implement. Two-dimensional (2D) layered semiconducting materials have become a focus of intense research due to their unique electrical and optical properties, high carrier mobilities, and tunable band gap [1]. These characteristics make them particularly interesting for optoelectronic applications, especially in photocurrent generation, photovoltaics, and light detection, where photon-induced charge carrier generation is a fundamental process.

Traditionally, photoresponse in 2D materials has been primarily explored through photocurrent generation, where light-induced charge carrier separation leads to measurable electrical current. For instance, in graphene field-effect transistors using a graphene/SiO_2/lightly-doped-Si structure, photogenerated carriers are separated by an electric field at the silicon/silicon oxide interface, leading to electron accumulation and a shift in the graphene's Fermi level, which enhances photocurrent [2]. Similarly, in monolayer MoS_2, photogenerated holes trapped at the MoS_2/SiO_2 interface dominate the photoresponse, with defect distribution playing a critical role in charge carrier dynamics [3].

The photovoltaic effect involves the direct conversion of light to electrical energy generating electron-hole pairs, and their splitting is facilitated by internal electric fields at p-n junctions or Schottky barriers, producing voltage and current without external bias [4–6]. Similarly, in photoconductive processes, incident photons with energy equal to or greater than the band gap generate free electron-hole pairs, increasing the electrical conductivity of a material [7]. Meanwhile, photogating, a

* Corresponding author.
E-mail address: raul@tpu.ru (R.D. Rodriguez).

https://doi.org/10.1016/j.apmt.2025.102592
Received 14 November 2024; Received in revised form 29 December 2024; Accepted 6 January 2025
Available online 18 January 2025

more complex case of the photoconductive effect, occurs when light-induced charge carriers become trapped in localized states, such as defects or interface states [4,8]. However, these conventional mechanisms represent only a subset of possible light-matter interactions in 2D materials, leaving room for new photoresponse phenomena that could enable new functionalities.

In this context, we introduce arsenic trisulfide (As_2S_3), a naturally occurring van der Waals (vdW) semiconductor, as a promising material for light-responsive applications. As_2S_3 exhibits remarkable optical properties, including giant in-plane optical anisotropy ($\Delta n \sim 0.4$) with zero optical losses, high refractive index ($\lambda < 620$ nm), and an optical band gap of $\sim$ 2.7 eV ($\lambda g \sim 460$ nm) within the visible range [9]. A unique mechanism of exciton-phonon interaction in As_2S_3 was recently reported, demonstrating that excitons and lattice dynamics are driven by ultrafast intrinsic excited state localization through interlayer bond formation [10]. This interaction leads to the formation of self-trapped excitons (STEs), which we hypothesized could act as localized dipoles under specific light conditions, enabling surface potential modulation without generating free charge carriers.

Our investigation provides new insights by demonstrating that As_2S_3 surface potential modulation is driven by STEs without generating free charge carriers. To our knowledge, there is no other material that displays this behavior demonstrating the diversity of photoresponse mechanisms possible in 2D materials.

We further demonstrate the practical implications by designing a plasmonic heterostructure with As_2S_3 and silver nanowires (AgNWs). We verified that the photocatalytic conversion of 4-nitrobenzenethiol (4-NBT) in the As_2S_3-AgNW system was enhanced due to the improved surface photoresponse of As_2S_3. This modulation boosted the plasmonic photocatalytic activity of AgNWs. This conversion serves as a model reaction to demonstrate photocatalytic efficiency enhancement by this photoresponse mechanism.

2. Methods

2.1. Materials

Bulk As_2S_3 mineral from a Siberian Russian quarry was used for mechanical exfoliation. Highly-oriented pyrolytic graphite (HOPG) (NT-MDT, Russia), Si/SiO_2 with an oxide layer of 100 nm (Telekom-STV, Russia) and, glass coated with a 100 nm layer of Indium Tin Oxide (ITO) were used as transfer substrates. Silver nanowires (AgNWs) were synthesized according to the protocol described by Wang *et al.* [11]. A 10^{-3} M solution of 4-nitrobenzenethiol (4-NBT) was prepared by mixing 7.75 mg 4-NBT in a 1:1 solution of distilled water and ethanol (25 mL each).

2.2. Sample preparation

Thin flakes were obtained by mechanical exfoliation (scotch tape method) of natural As_2S_3 crystals. These flakes were then transferred onto three different substrates: (1) HOPG for the optical, Raman, SEM, and AFM analysis, (2) Si/SiO_2 for control analysis, and (3) ITO-glass for control analysis and experiments with 4-NBT. To facilitate electrical contact for electrical AFM modes, the HOPG and Si/SiO_2 substrates were electrically connected to a copper substrate using silver paste, and a copper wire was attached to this substrate. The copper wire was directly connected to the ITO-glass substrate. The flakes used in all the experiments were from the same crystal.

For the photocatalysis experiment, <10 μL of AgNWs dispersion was drop-casted on the As_2S_3/ITO-glass, resulting in the AgNWs/As_2S_3/ITO-glass sample.

2.3. SEM characterization

SEM images were collected using an SU8000 scanning electron microscope (Hitachi High-Tech, Japan) operating at 15 kV accelerating voltage.

2.4. XRD characterization

XRD spectra were obtained with a Rigaku SmartLab SE Discover high-resolution diffractometer equipped with a 9 KW rotating anode X-ray tube and a double-bounce Ge (220) monochromator. The spectra were acquired in the 2θ range from 10 to 60° on a glass substrate.

2.5. UV–Vis

Diffuse reflectance spectra (DRS) were recorded using a Thermo Scientific Evolution 600 UV–Vis spectrophotometer (England) in the wavelength range of 190–900 nm. The sample preparation involved grinding As_2S_3 into a fine powder to ensure uniformity and to minimize scattering effects. Bandgap energies were calculated by applying the modified Kubelka–Munk function (F(R∞)) to the DRS data. The direct band gap was estimated from $(h\nu F(R\infty))^2$ and the indirect from $(h\nu F(R\infty))^{1/2}$ versus $h\nu$. Spectra were collected with a spectral bandwidth of 2 nm.

2.6. Optical microscopy and Raman spectroscopy

Raman spectroscopy was employed to analyze the vibrational properties of the As_2S_3 flakes. Spectra were acquired using a Raman microscope (NTEGRA Spectra, NT-MDT SI, Russia) equipped with 457, 532, and 633 nm lasers. A 100 × objective lens (Mitutoyo, NA 0.70) was used to focus the laser on the sample surface. The scattered light was collected by an electron-multiplying charge-coupled detector (EMCCD) (Andor Newton, UK) cooled to −65°C. All spectra were calibrated using the 520.7 cm^{-1} line of a silicon wafer as a reference. The optical setup of the Raman microscope was used to image the As_2S_3 flakes and locate the regions of interest.

Raman mapping was utilized to visualize the distribution of 4-NBT and its photocatalytic reaction product on the AgNWs/As_2S_3/ITO-glass sample. The acquisition time was set to 0.4 seconds, capturing an image size of 20 × 20 μm^2 with a 20 × 20 points resolution. This setup provided a detailed spatial distribution of the molecular interactions using a 532 nm laser. The maps were obtained with 100 × objective, with a laser power of 21.7 μW. For single Raman spectra, the same parameters were used, but the acquisition time was set to 30 seconds. All measurements were performed at room temperature (RT) (28–32°C).

2.7. AFM and electrical AFM modes measurements

Atomic force microscopy (AFM) measurements were conducted using an NTEGRA AFM system (NT-MDT, Russia) at RT, with voltage applied to the sample and a grounded tip. For reproducibility, additional KPFM experiments used an NTEGRA Spectra II AFM-Raman microscope (NT-MDT SI, Russia) in the same configuration.

The morphology and thickness of the As_2S_3 flakes were characterized in a tapping mode AFM with Si cantilevers NSG10 (NT-MDT, Russia). Various electrical AFM modes were employed, including Kelvin Probe Force Microscopy (KPFM), Electrostatic Force Microscopy (EFM), and Scanning Capacitance Microscopy (SCM) conducted in tapping mode, as well as Current Sensing Atomic Force Microscopy (CS-AFM) in contact mode. All electrical measurements were performed using platinum (Pt)-coated Si cantilevers. For KPFM, EFM and SCM NSG10/Pt cantilevers (NT-MDT, Russia) with spring constant 3.1–37.6 N/m were used, while CSG30/Pt (NT-MDT, Russia) and home-made gold tips were used for CS-AFM.

These AFM electrical measurements were obtained under various illumination conditions: (1) dark; (2) white light illumination from the integrated video microscope of the AFM system (see lamp spectrum in Figure S1(a)); (3) blue light illumination at an incident angle of 20° using a 450 nm diode laser at varying powers; and (4) red light

illumination at an incident angle of 20° using a 638 nm diode laser, also at varying powers.

2.8. Photocatalysis experiment

To investigate the photocatalytic properties of As_2S_3, 4-NBT was used as a model compound. The AgNWs/As_2S_3/ITO-glass sample was immersed in a 4-NBT solution for 4 hours. After immersion, the sample was washed with distilled water to remove any excess 4-NBT. The treated sample was then analyzed using Raman spectroscopy to assess the photocatalytic activity of As_2S_3.

3. Results and discussion

3.1. General characteristics

Arsenic trisulfide (As_2S_3) occurs in both amorphous and crystalline forms [9]. The crystalline form, orpiment, occurring naturally, exhibits a low-symmetry (monoclinic) layer structure. The weak van der Waals (vdW) forces between these layers result in a low exfoliation energy (0.28 J/m^2, lower than graphite), facilitating mechanical exfoliation down to the monolayer level [12]. To avoid issues associated with poor air stability in monolayers, in this study, we focus on few-layer As_2S_3 flakes with thicknesses below 20 nm.

Figure 1(a) shows a picture of the As_2S_3 crystal used in this study, highlighting its distinctive bright golden-yellow color, which made it so attractive as a pigment in artworks. Figure 1(b) illustrates the simplified crystal structure, exhibiting AsS_3 pyramids interconnected through shared sulfur atoms to form layers oriented parallel to the (010) plane. The structural integrity of the As_2S_3 layered structure is attributed to the weak vdW interactions between As-S, S-S, and As-As pairs [13]. As_2S_3 possesses a *Pmn2$_1$* symmetry, characterized by a mirror reflection to the *xz*-plane and a lack of symmetry with the *yz*-plane, facilitating spontaneous electric polarization along the *x*-axis [14]. X-ray diffraction (XRD) analysis confirmed the crystalline structure of As_2S_3. The diffraction pattern exhibited characteristic peaks at 2θ = 18.4°, 20.0°, 22.2°, 24.1°, 28.0°, 29.0°, 32.1°, 33.0°, 35.1°, 36.7°, 37.5°, 38.4°, 43.3°, 44.7°, 52.3°, and 57.7°, corresponding to the (020), (−101), (021), (130), (040), (311), (330), (140), (041), (−202), (051), and (060) crystallographic planes of the monoclinic structure [15,16] (Figure S2). The strong (020) peak intensity indicates the preferred orientation along the crystal's natural cleavage plane, consistent with its layered structure.

The SEM image in Figure 1(c) shows the As_2S_3 layered structure. The topography and thicknesses of the As_2S_3 flakes were analyzed with AFM, as shown in Figure 1(d), for an exfoliated As_2S_3 flake on highly oriented pyrolytic graphite (HOPG) with a thickness of 325 nm. In our study, we investigated As_2S_3 with different thicknesses, ranging from a few layers (3–5 layers) to multilayers (6–19 layers) and thicker bulk samples (20+ layers). Figure S3 displays an AFM image of exfoliated As_2S_3 flakes with thicknesses ranging from monolayer to a few layers. The inset line profile shows thickness measurements for monolayer (0.8 ± 0.1 nm), bilayer (1.6 ± 0.1 nm), and trilayer (2.4 ± 0.1 nm) flakes, closely matching values reported by Šiškins *et al.* [17]. These results show a mismatch between the experimental monolayer thickness and the theoretical value of 0.48 nm [17,18]. This mismatch between expected and AFM-measured layer thickness has been observed for other 2D materials and attributed to adsorbed water layers, intercalation, surface roughness, and differences in tip-sample interaction [19,20].

The Raman spectrum of a few-layer As_2S_3 in Figure 1(e) reveals characteristics of As–S bands at 355, 310, and 292 cm^{-1}, with the most intense band at 355 cm^{-1}, followed by a second intense band at 310 cm^{-1} [21]. Additionally, other lower-intensity bands were observed at 380, 200, 155, and 135 cm^{-1}. These seven Raman vibrational modes match previous literature reports, confirming the chemical composition and structural integrity of the material [17,21].

Inspired by recent studies reporting giant optical anisotropy [9] and strong exciton-lattice interactions in As_2S_3 [10], we hypothesized that this material should display unique optoelectronic properties under illumination. In particular, the strong exciton localization reported by Li *et al.* implies that the electronic properties of this material could be modulated by light [10]. To test this hypothesis, we conducted photo-Kelvin probe force microscopy (KPFM) experiments. The results, shown in Fig. 1(f), reveal a significant increase in the contact potential difference (CPD) under light illumination, confirming a photoresponse in As_2S_3. Fig. 1(g) presents a CPD profile that clearly demonstrates these light-induced changes, inciting further investigation into the mechanisms behind this photoresponse.

3.2. Electronic characterization

We investigated the photoresponse of As_2S_3 through advanced AFM techniques, including KPFM, EFM, and SCM. These methods provide complementary insights into the surface potential variations, charge distribution, and capacitance changes in As_2S_3 under different conditions. Fig. 2(a) shows a basic schematic of the AFM measurement setup for topography and KPFM. In the first pass, the topography is recorded in semi-contact mode. In the second pass, the tip is lifted 10 nm, and a voltage is adjusted to nullify electrostatic forces, allowing the CPD to be determined (see Supplementary Note 1 for more details). Optical and AFM topography images in Fig. 2(b) and Fig. 2(c) reveal a well-defined triangular-shaped As_2S_3 flake with a thickness of ~17 nm. The underlying topography of the HOPG substrate is visible through the As_2S_3 flake due to strong interactions between the two materials, which is one of the reasons we chose HOPG as a substrate in addition to its electrical conductivity [22].

For KPFM measurement, using a Pt-coated tip as a reference and an As_2S_3 flake on HOPG as the target material, we calculated the work function through V_{CPD} measurements (Equation 5 in Supplementary Note 1) [23]. To verify the stability of the tip's work function, we acquired CPD maps on HOPG and SiO_2/Si substrates switching under and dark and illuminated conditions (Figure S4). The stability of the CPD values confirms the Pt tip's reliability as a reference regardless of light conditions.

Using HOPG's work function as reference [24] and V_{CPD} value under dark (Supplementary Note 1), we determined the Pt-coated tip work function at 4.82 eV in agreement with literature values [25]. A similar analysis using the tip as a reference yielded a work function of 4.53 eV for As_2S_3. This value is comparable to the 4.67 eV reported for bulk As_2S_3 [26], with the difference likely due to the nanoscale thickness of our layers [27].

Next, we investigated how As_2S_3's CPD changes under illumination. Fig. 2(d-f) presents two CPD maps and profiles of the As_2S_3 flake, CPD_{light}, and CPD_{dark} with and without illumination, respectively. This comparison enables us to evaluate the changes in CPD (ΔCPD) as follows:

$$\Delta CPD = CPD_{light} - CPD_{dark} \quad (1)$$

The CPD profiles along the *x*-axis clearly visualize the photoinduced ΔCPD. Upon illumination, the HOPG substrate showed an increase of less than 40 mV (from 217 ± 5 mV to 255 ± 6 mV). Interestingly, the HOPG substrate's CPD is modulated under illumination in the presence of As_2S_3. To verify this effect, we conducted KPFM measurements on both SiO_2 and HOPG substrates under alternating illumination (Figure S5). This modulation was less pronounced on SiO_2, likely due to its wide bandgap energy (E_G= 9 *eV*) [28], which exceeds the energy of visible light photons or the differences in intrinsic charge carrier density polarized by As_2S_3 that persist when the tip extends beyond the flake.

In the case of As_2S_3 the CPD value changed by 80 ± 8 mV (from 291 ± 5 mV to 371 ± 6 mV). This CPD increment implies that the work function of As_2S_3 under illumination decreased from 4.53 ± 0.01 eV to 4.45 ± 0.01 eV. This change corresponds to a Fermi level upshift (closer to the vacuum level) as more electrons are excited to higher energy

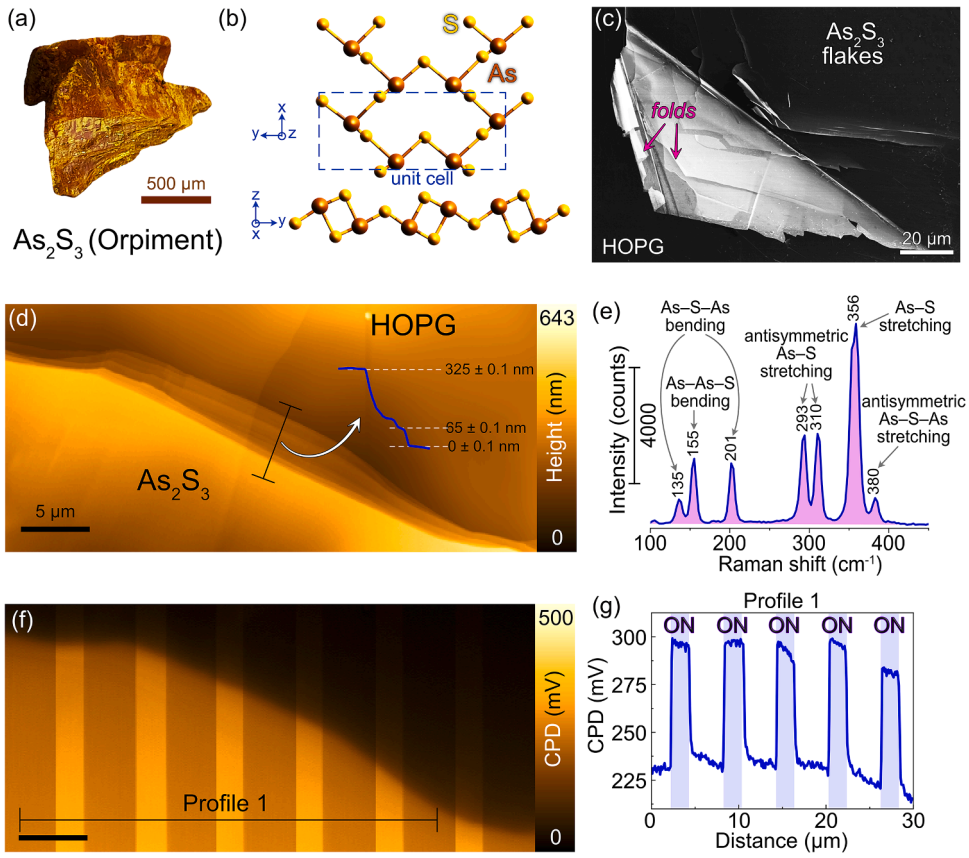

Fig. 1. Structural, spectroscopic, and photoelectric characteristics of As_2S_3 flakes. (a) Image of the natural orpiment mineral used in this study. (b) Schematic diagram of As_2S_3 crystal structure, showing the projection of lattice along the *z*-axis and *x*-axis. The darker balls represent As atoms, and the lighter ones S atoms. As atoms in the crystal are three-fold coordinated and bonded to two-fold coordinated S atoms. The dotted line shows the unit cell. (c) SEM image of As_2S_3 on HOPG, reveals visible steps formed layer by layer and folds due to transfer process. (d) AFM image of an exfoliated As_2S_3 flake on HOPG with a height profile showing thickness from 65 nm to 325 nm. (e) Raman spectrum of As_2S_3, highlighting its distinctive vibrational modes. The data were acquired using a 532 nm laser. (f) KPFM image showing the CPD of As_2S_3 with and without illumination of (d). (g) CPD profile along the black line in (f), demonstrating the response to multiple sequences of light on/off cycles. The plot shows consistent light-induced changes in the sample's surface potential.

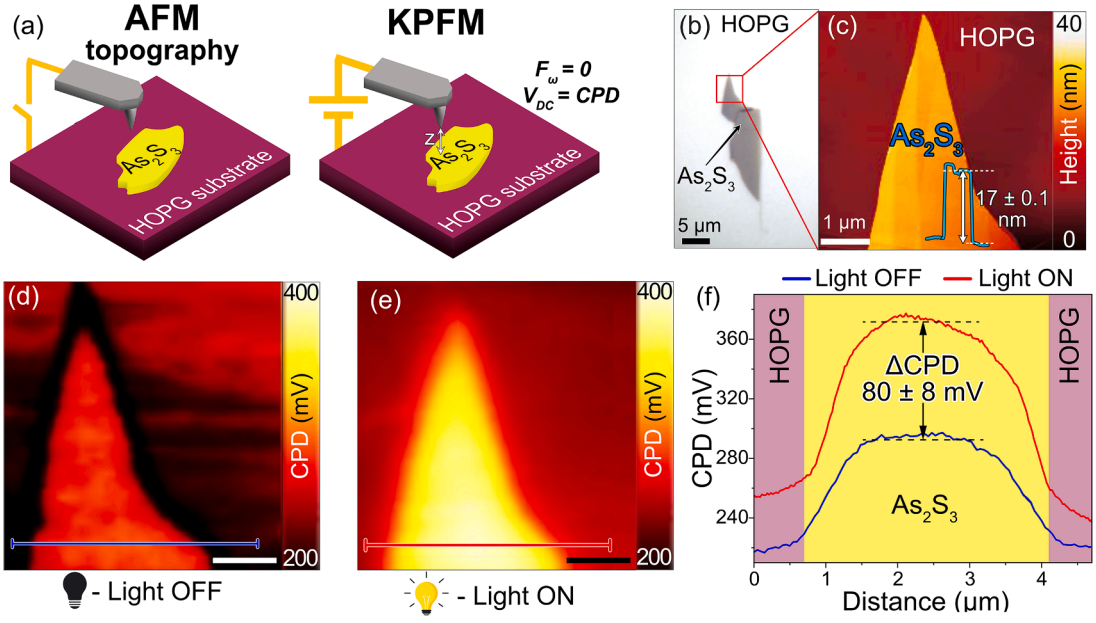

Fig. 2. Photoinduced surface potential changes in As_2S_3 flakes on HOPG substrate. (a) Schematic representations of AFM-based technique. (b) Optical image and (c) AFM topography of As_2S_3 flake and its step height profile in the inset. (d-f) KPFM images and their respective CPD profiles in illuminated and dark states along the *x*-axis. Scale 1 μm.

levels [29], demonstrating high photosensitivity in As_2S_3.

KPFM measurements under alternating illumination conditions, conducted using two AFM systems, showed higher photoresponse in As_2S_3 when using equipment N°2 as shown in Figure S6, which we attribute to its higher-intensity halogen lamp (Figure S1(b)). Despite the variation in illumination intensity between systems, the CPD ratios of As_2S_3 relative to HOPG remained consistent: 1.3 in dark conditions and 1.5 under illumination for both systems (Table S1), confirming device-to-device reproducibility. KPFM measurements conducted on As_2S_3 flakes of varying thicknesses (Figure S7 and Figure S8(a-e)) revealed that the CPD response to illumination increases with sample thickness, with bulk As_2S_3 showing the strongest effect. This thickness-dependent photoresponse suggests a correlation between the number of layers and the CPD magnitude, possibly due to dipole moment superposition across layers.

To deepen our understanding of the As_2S_3 photoresponse, we characterized the CPD wavelength dependence under various light sources: white light (Fig. 3(a)), blue laser (Fig. 3(b)), and red laser (Fig. 3 (c)). For each light source, we first measured a CPD baseline in the dark for 46 seconds, followed by 46 seconds of illumination. Then, we turned off the light and continued the CPD measurements for 369 seconds to observe the relaxation dynamics.

The CPD maps show that these wavelengths interact differently with As_2S_3. This difference is mainly due to photon energy for each light source relative to the direct and indirect optical band gaps, which we measured to be ~2.50 eV and ~2.39 eV, respectively, using UV–Vis DRS (Figure S9). These values are consistent with previously reported values of ~ 2.6 and 2.4 eV, respectively [10]. Shorter wavelengths drive interband transitions, while longer-wavelength photons excite specific low-energy states within the band gap. According to Li *et al.*, interband transitions in As_2S_3 lead to the formation of STEs due to strong exciton-phonon coupling and lattice distortions [10]. These distortions

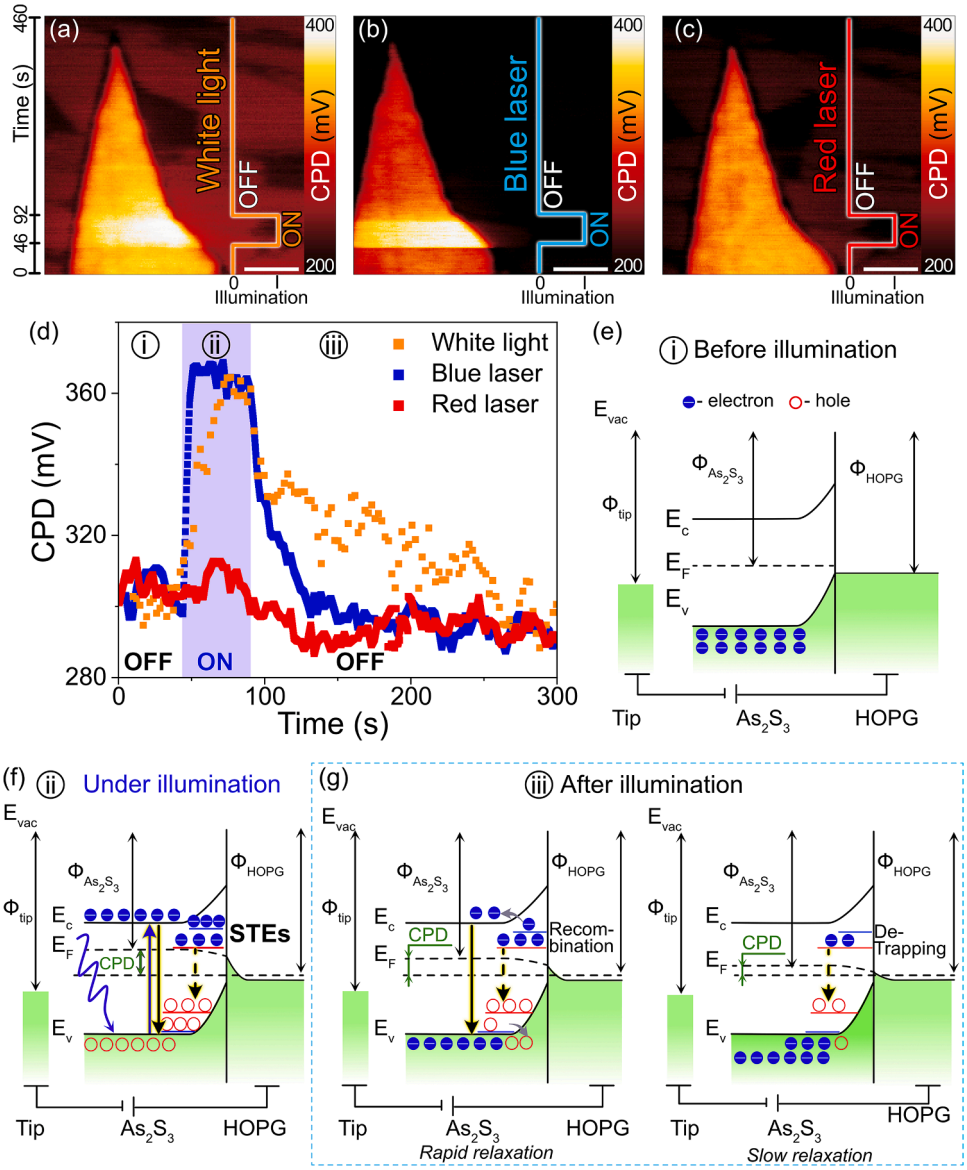

Fig. 3. Evolution of surface potential of As_2S_3 under various light sources. (a) white light, (b) blue laser (450 nm, 1.1 mW; maximum tested power of 4.35 mW produced similar results), and (c) red laser (638 nm, 3.57 mW). As_2S_3 flake thickness ~17 nm. Scale bar 1 μm. (d) Comparative temporal CPD dynamics under different illumination sources from (a,b,c). (e) Energy band diagrams of As_2S_3. The energy band diagrams correspond to the stages in (d) (1) before, (2) under and, (3) after illumination. The vertical axis illustrates the work function of the tip, As_2S_3 and HPOG, aligned to the vacuum level (E_{vac}). The horizontal dotted lines denote the Fermi levels (E_F). KPFM measurements align the E_{vac} to determine work function differences. E_v and E_c represent the valence band and conduction band edges, respectively.

lead to a reduction in the interlayer distance, forming partial bonds between sulfur atoms that trap excited electron-hole pairs, lifting the Fermi level and thereby increasing the CPD. Therefore, CPD modulation occurs only when STEs are formed, which requires the absorption of photons with energy large enough to excite interband transitions. This explains why CPD modulation occurs under white light and blue laser (450 nm) with photon energies above the band gap. In contrast, the red laser (638 nm) has an energy below the band gap, resulting in negligible STE formation and no CPD modulation (Fig. 3(c)).

To gain further insights into the photoresponse mechanism, we analyzed the temporal CPD dynamics under these illumination sources. Fig. 3(d) shows the three stages of the photoresponse: (i) before illumination (dark state), (ii) during illumination (photoexcited state), and (iii) after illumination (relaxation state). The corresponding band diagrams are presented in Fig. 3(e-g).

3.2.1. Photoexcited state

Initially, in the dark, the CPD of the As_2S_3/HOPG system remains stable at 300 mV, as indicated by the flat sections of the plots in Fig. 3(d), labeled (i). This "dark state" represents the equilibrium condition of the system before any photoexcitation. The energy band diagram for this state is shown in Fig. 3(e).

We then illuminated the sample for 46 seconds with each of the three light sources (Figure 3(d)), obtaining the CPD vs. time curves labeled (ii). These results show that As_2S_3 has a wavelength-dependent photoresponse, which can be explained by the different electron excitation and trapping processes, as illustrated in Fig. 3(f).

Upon photoexcitation, the photogenerated carriers can either recombine and return to the ground state or become trapped after transferring energy to the lattice. This energy transfer distorts the lattice, creating STEs with a lifetime of nanoseconds [10] that act as localized dipoles. These exciton dipoles result in an increase in CPD due to the upshift in the Fermi level, which also depends on the As_2S_3 response to different light sources as follows:

- **White light:** As_2S_3 shows a gradual increase in CPD from its initial dark state value of 300 mV, reaching ~344 mV after about 10 seconds. This occurs despite the low power density and continuous emission spectra with a maximum at 600 nm (see Figure S1(a)), allowing for the slow filling of exciton states in the band gap.
- **Blue laser illumination (450 nm):** As_2S_3 displays a sharp and immediate response, with the CPD value quickly reaching ~ 365 mV in about 4 seconds and remaining stable. This rapid change occurs because the blue laser's energy closely matches the optical band gap of As_2S_3 at ~ 2.7 eV (λg ~ 460 nm) [9], efficiently generating STEs. To confirm this behavior, we conducted experiments using a 450 nm laser at different optical powers (Figure S10) and calculated the rise time (τr). The τr values at 1.1 mW and 4.35 mW were found to be 3.98 and 1.84 seconds, respectively, demonstrating a decrease in τr with increasing optical power. Moreover, the CPD plateau of As_2S_3 increases with power since more STEs get excited, and so do more dipoles.
- **Red laser illumination (633 nm):** No detectable changes in CPD values were observed. This lack of photoresponse is due to the photon having energy below the As_2S_3 band gap being insufficient to generate STEs.

These distinct responses to different light wavelengths, particularly the sharp and immediate response to blue laser illumination and the lack of response to red laser illumination, imply that the CPD changes are directly linked to electronic interband transitions given rise to STEs, rather than other possible effects like photothermal heating and lattice expansion.

When the rate of photogeneration equals the rate of recombination of charge carriers, the CPD stabilizes, reaching a plateau under white light and blue laser illumination. This indicates a steady state between excitation, trapping, and relaxation processes. The trapped carriers, as shown in Fig. 3(f), prevent immediate recombination, contributing to the stability of the photoresponse and maintaining the CPD value until the light is turned off.

3.2.2. Relaxation state

When the illumination is switched off (Fig. 3(d), labeled (iii)), a two-phase relaxation process occurs (Fig. 3(g)). First, a rapid decrease in CPD is attributed to the recombination of exciton, the energy state of which is close to the conduction band minimum, followed by a slower relaxation due to the release of charges from trap states.

The relaxation dynamics vary depending on the illumination source. Relaxation after white light illumination is slower, with an exponential time constant of 37 seconds, compared to blue laser illumination, with a time constant of 19 seconds. This difference in time constants is likely due to the broader emission spectrum of white light populating a wider range of trap states.

The charge-carrier recombination and de-trapping mechanism in semiconductors are complex and influenced by various factors, including trap characteristics, temperature, and environmental conditions, with carrier release time from traps exceeding the duration of the initial trapping process [30]. Structural defects, such as vacancies, adatoms, substitutional impurities, and grain boundaries, can act as recombination centers [31,32], affecting the relaxation dynamics observed in As_2S_3.

The interplay between structural defects and relaxation processes was reported in other 2D materials like ReS_2, where engineered trap states enhance photodetector performance [33]. In that study, three relaxation stages were observed after green laser (532 nm) illumination: rapid recombination of excess carriers, followed by the emptying of shallow traps, and finally, the emptying of deep traps. This multi-stage relaxation process and the 200-second relaxation time reported by Jiang *et al.* [33] align with our observations under white light illumination, suggesting the impact of carrier traps in the relaxation dynamics of As_2S_3.

To further investigate the photoresponse mechanism of As_2S_3, we used other AFM techniques, including EFM, SCM, and CS-AFM, as shown in Figure S8(f-g) and Figure S11(a) (for further details, see Supplementary Note 2). Additionally, we conducted electrical measurements using an interdigitated electrodes (IDEs) configuration.

Interestingly, CS-AFM and IDE measurements showed no response to light (Figure S11). The absence of photocurrent in these measurements ruled out photoconductive and photovoltaic effects as the primary mechanisms behind the observed photoresponse in KPFM, pointing towards a photo-induced dipole effect as the photoresponsivity driver.

Li *et al.* demonstrated the presence of STEs in As_2S_3 due to ultrafast intrinsic excited state localization [10]. Self-trapping occurs when photoexcited electrons and holes spontaneously transfer energy to the lattice, creating distortions that localize and trap the carriers [34]. These STEs act as localized dipoles affecting the surface potential but not the long-range conductivity because of their limited mobility.

To investigate the charge carrier density or mobility, we employed oscillation amplitude versus V curves in SCM measurements (Figure S12). The findings revealed that the amplitude remained stable at approximately 26.15 nA during voltage sweeps without illumination, indicating consistent carrier density (Figure S12(a)). Upon illumination at 9 minutes, the amplitude increased to 26.4 nA, suggesting charge carrier generation. However, at 12 minutes, the amplitude returned to 26.15 nA, indicating that all generated charge carriers were trapped within 3 minutes. During sweeps at 12 and 15 minutes, the amplitude gradually decreased due to trapping by photogenerated traps resulting from lattice distortion (Figure S12(b)). After turning off the light at 18 minutes, the forward sweep exhibited a 0.4 nA difference (twice the value observed under illumination) reflecting the absence of new charge carrier generation and the long lifetime of unoccupied traps. In the backward curve at 18 minutes, there was little change in amplitude,

suggesting a balance between trapping and detrapping processes. Subsequent measurements at 21 and 24 minutes indicated an increase in amplitude due to a dominant de-trapping process and a decrease in unoccupied traps (Figure S12(c)).

Our investigation of As_2S_3 using advanced AFM techniques has revealed a unique photoresponse driven by STEs. This photoresponse exhibits strong wavelength dependence, with blue light (450 nm) inducing rapid and pronounced changes, while red light (638 nm) shows no detectable response. Despite significant CPD modulation with light, we observed no measurable photoconductivity in CS-AFM studies, indicating that the photoresponse results in STEs instead of free charge carriers. SCM further supports this hypothesis, revealing constant carrier concentration and evidencing the localized nature associated with STEs and unoccupied traps induced by lattice distortion. To provide further context and benchmark our findings, Table S2 in the Supporting Information compares photoresponse mechanisms, experimental methods, and key outcomes from recent studies of other 2D materials. This photoresponse mechanism in As_2S_3, where light-induced STEs generate local dipole moments that modulate the material's surface potential, opens up possibilities in applications such as phototransistors, sensors, and photocatalysis. As an illustration of these opportunities, in the next section, we explore using As_2S_3 to modulate and enhance photocatalytic processes.

3.3. Boosting photocatalytic conversion

To explore the potential applications of the unique photoresponse of As_2S_3, we investigated the photocatalytic reduction of 4-NBT to 4,4′-dimercaptoazobenzene (DMAB) [35] in a hybrid system with AgNWs on an ITO substrate. We hypothesized that the As_2S_3 photoresponse would create a localized electric field, modulating and enhancing the photocatalytic properties of AgNWs.

Fig. 4 shows the KPFM and Raman hyperspectral imaging results, revealing the light-induced surface potential modulation of AgNWs and photocatalytic activity of the AgNWs/As_2S_3/ITO system. Fig. 4(a) shows the AFM topography of an AgNW on the As_2S_3 surface. Fig. 4(b) shows the CPD image under periodic illumination, light ON and light OFF, as illustrated in the sketch (Fig. 4(c)). We strategically employed a green laser (532 nm), to demonstrate the CPD modulation capacity of photon energy below the As_2S_3 band gap (Figure S13).

When illuminated, photogenerated charge carriers trapped in As_2S_3 create a local electric field that modulates the material's surface potential, as evidenced by the changes in CPD. A key observation is that the light-induced modulation is not confined to As_2S_3's CPD but also extends to the AgNWs on its surface. This modulation is a direct manifestation of the photo-dipole effect in As_2S_3, suggesting a strong electronic coupling with AgNWs, potentially enhancing their catalytic activity.

The CPD profile across the AgNW (inset in Fig. 4(c)) shows an increase in surface potential at the AgNW/As_2S_3 interface, suggesting that this junction plays a crucial role in surface polarization. The AFM topography image in Fig. 4(d) shows AgNWs dispersed throughout the sample, with the As_2S_3 flake exhibiting a 219.1 ± 8.5 nm thickness. The corresponding Raman map in Fig. 4(e) from the same location demonstrates the surface-enhanced Raman spectroscopy effect by AgNWs on top of As_2S_3. The Raman map shows the intensity of the A_g (353 cm^{-1}) mode from As_2S_3 [36] and the DMAB mode (1434 cm^{-1}) [37], which is confined at the ends of the AgNWs. This localized spatial correlation shows that the AgNWs tips act as preferential catalytic sites, likely due to a higher electric field enhancement at these locations that promotes charge transfer and catalytic conversion. Fig. 4(f) displays the Raman spectra corresponding to points of interest 1, 2, 3, and 4 marked in the AFM and Raman images (Figs. 4(d) and 4(e)). Spectra 3 and 4 show the characteristic Raman band $\nu s(NO_2)$ of 4-NBT (1335 cm^{-1}) and the vibrational modes of the DMAB product (1138 cm^{-1} and 1388 cm^{-1}) [37, 38]. These results show that DMAB peaks dominate spectrum 4 due to the high photocatalytic efficiency conversion of 4-NBT (Fig. 4f). In contrast, the conversion of AgNWs in ITO was not as efficient, as evidenced by the persistence of the $\nu s(NO_2)$ of the 4-NBT peak in spectrum 3.

These results confirm that the photo-dipole effect in As_2S_3 enhances the photocatalytic conversion of 4-NBT to DMAB on AgNWs, resulting in high catalytic efficiency, as evidenced by the increased DMAB formation

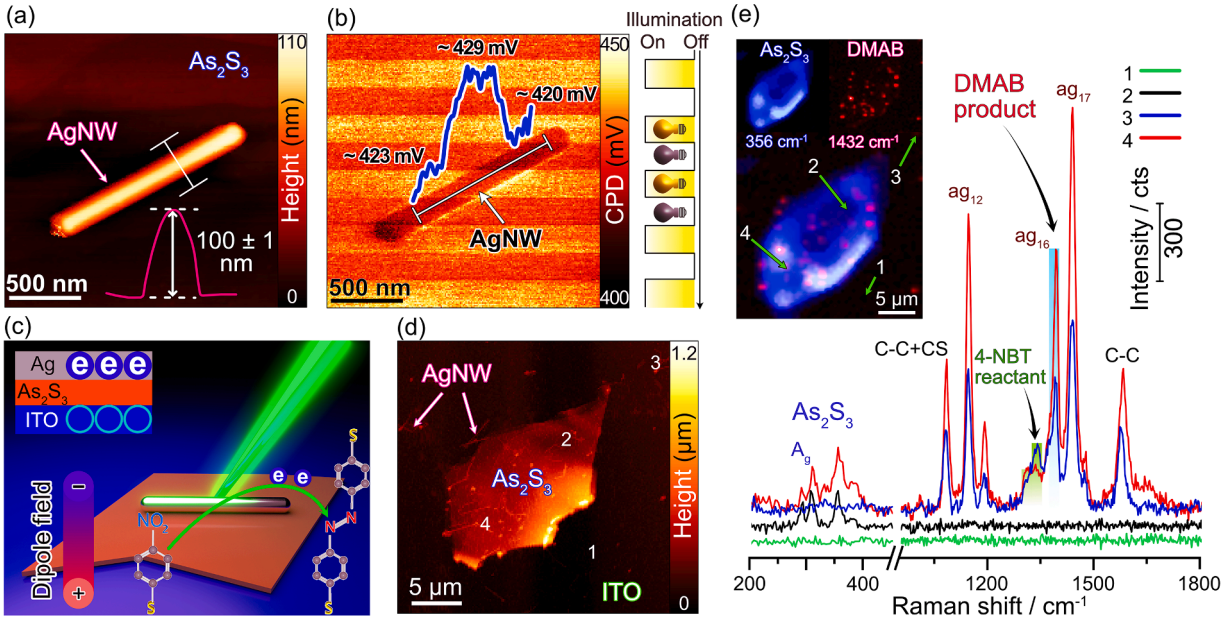

Fig. 4. Light-induced surface potential modulation and photocatalytic characterization of the AgNWs/As_2S_3/ITO system. (a) AFM topography image of an AgNW on As_2S_3 and its corresponding height profile in the inset. (b) KPFM image showing CPD distribution under varying white light illumination conditions (illumination sequence shown on left); inset shows CPD profile across the AgNW. (c) Schematic representation of the photo-dipole effect in the AgNWs/As_2S_3/ITO system and its impact on the photocatalytic reduction of 4-NBT to DMAB. (d) AFM topography image of AgNWs/As_2S_3/ITO-glass sample. (e) Raman map of (d) showing spatial distribution of As_2S_3 (blue) and photocatalytically produced DMAB (red). Right: Raman spectra for points 1–4, highlighting peaks of As_2S_3, 4-NBT (reactant), and DMAB (product). 1 - ITO (green), 2 - As_2S_3 (black), 3 - AgNWs/ITO-glass (blue), 4 - AgNWs/As_2S_3/ITO-glass (red). Scale bar 5 µm (d,e).

observed in our Raman spectroscopy experiments.

4. Conclusion

This study elucidated the unique photoresponse in two-dimensional arsenic trisulfide (As_2S_3), a naturally occurring van der Waals semiconductor. Our findings revealed a wavelength-dependent light-induced surface potential driven by the formation of self-trapped excitons. These STEs generate up to 80 mV under white light illumination without inducing free charge carriers, making As_2S_3 a promising photoresponsive material. We leveraged this photo-dipole effect to enhance the photocatalytic activity of silver nanowires. The localized electric field generated by the STEs in As_2S_3 boosted the conversion of 4-nitrobenzenethiol to 4,4′-dimercaptoazobenzene by 71 % compared to the AgNWs alone, highlighting this natural 2D material's potential for developing efficient photocatalytic systems. We anticipate future investigations, including Schottky emission analysis and ultrafast absorption spectroscopy, to elucidate details on the carrier dynamics in this exciting 2D system.

The photo-dipole effect, combined with As_2S_3's natural abundance and facile exfoliation, makes it an attractive material for various light-sensitive applications. In particular, the ability to modulate surface potential without generating free charge carriers could be exploited in devices such as phototransistors, optical switches, and plasmonic sensors, where precise control of local electric fields with light is crucial.

CRediT authorship contribution statement

Aura Garcia: Writing – review & editing, Writing – original draft, Visualization, Investigation, Funding acquisition, Formal analysis. **Raul D. Rodriguez:** Writing – review & editing, Writing – original draft, Methodology, Investigation, Formal analysis, Conceptualization. **Tuan-Hoang Tran:** Writing – review & editing, Visualization, Investigation, Formal analysis. **Dmitry Cheshev:** Writing – review & editing, Investigation, Formal analysis. **Nelson E. Villa:** Writing – review & editing, Writing – original draft, Investigation, Formal analysis. **Daria Gorbunova:** Writing – review & editing, Investigation. **Lyubov Krasnoshchekova:** Writing – review & editing, Resources. **Hao Liu:** Writing – review & editing, Investigation. **Bin Yang:** Writing – review & editing, Investigation. **Xin Jia:** Writing – review & editing, Investigation. **Qiang Ma:** Writing – review & editing, Investigation. **Tao Zhang:** Writing – review & editing, Investigation. **Jin-Ju Chen:** Writing – review & editing, Formal analysis. **Evgeniya Sheremet:** Writing – review & editing, Formal analysis.

Declaration of competing interest

The authors declare that they have no known competing financial interests or personal relationships that could have appeared to influence the work reported in this paper.

Acknowledgments

This study was primarily supported by the TPU Postdoctoral Research Funding (Priority-2030-NIP-026–202–2024) for Aura Garcia. Bin Yang acknowledges support from the National Natural Science Foundation of China (22308223), the High-level Talents launching Project (RCZK202328), and Xinjiang Uygur Autonomous Region Tianchi Talent Introduction Program (Young Doctor). Additionally, this research benefited from contributions by the National Natural Science Foundation of China (U1703351, 52073179), the Tiansh an Talent Support Program for Xin Jia, and the Program of Introducing Talents of Discipline to Universities (D20018). Jin-Ju Chen acknowledges the support provided by the Chengdu Science and Technology Program (grant No. 2023-GH02–00021-HZ) and Sichuan Science and Technology Program (grant No. 2023YFG0215).

This work would not have been possible without the kind provision of the mineral samples used in this study by Olesya Savinova. The authors thank the School of Earth Sciences and Engineering at TPU and Artem Boev for granting access to the mineral resources investigated in this study. The authors also gratefully acknowledged Maxim Fatkullin from TPU, for fruitful discussions and comments on the manuscript. Lastly, we thank Nikolay B. Egorov from TPU for conducting DRS measurements.

Supplementary materials

Supplementary material associated with this article can be found, in the online version, at doi:10.1016/j.apmt.2025.102592.

Data availability

Data will be made available on request.

References

[1] S. Kang, D. Lee, J. Kim, A. Capasso, H.S. Kang, J.-W. Park, C.-H. Lee, G.-H. Lee, 2D semiconducting materials for electronic and optoelectronic applications: potential and challenge, 2d Mater. 7 (2020) 022003.
[2] X. Guo, W. Wang, H. Nan, Y. Yu, J. Jiang, W. Zhao, J. Li, Z. Zafar, N. Xiang, Z. Ni, W. Hu, Y. You, Z. Ni, High-performance graphene photodetector using interfacial gating, Optica 3 (2016) 1066.
[3] W. Yim, V.T. Nguyen, Q.T. Phung, H.S. Kim, Y.H. Ahn, S. Lee, J.-Y. Park, Imaging spatial distribution of photogenerated carriers in monolayer mos with kelvin probe force microscopy, ACS Appl. Mater. Interfaces 14 (2022) 26295–26302.
[4] M. Buscema, J.O. Island, D.J. Groenendijk, S.I. Blanter, G.A. Steele, H.S.J. van der Zant, A. Castellanos-Gomez, Photocurrent generation with two-dimensional van der Waals semiconductors, Chem. Soc. Rev. 44 (2015) 3691–3718.
[5] H. Fang, W. Hu, Photogating in Low Dimensional Photodetectors, Adv. Sci. 4 (2017) 1700323.
[6] R. Dutta, A. Bala, A. Sen, M.R. Spinazze, H. Park, W. Choi, Y. Yoon, S. Kim, Optical enhancement of indirect Bandgap 2D transition metal dichalcogenides for multi-functional optoelectronic sensors, Adv. Mater. 35 (2023) e2303272.
[7] K.W. Böer, U.W. Pohl, Photoconductivity. Semiconductor Physics, Springer International Publishing, Cham, 2023, pp. 1299–1324.
[8] A. Di Bartolomeo, A. Kumar, O. Durante, A. Sessa, E. Faella, L. Viscardi, K. Intonti, F. Giubileo, N. Martucciello, P. Romano, S. Sleziona, M. Schleberger, Temperature-dependent photoconductivity in two-dimensional MoS2 transistors, Mater. Today Nano (2023) 100382.
[9] A.S. Slavich, G.A. Ermolaev, M.K. Tatmyshevskiy, A.N. Toksumakov, O. G. Matveeva, D.V. Grudinin, K.V. Voronin, A. Mazitov, K.V. Kravtsov, A.V. Syuy, D. M. Tsymbarenko, M.S. Mironov, S.M. Novikov, I. Kruglov, D.A. Ghazaryan, A. A. Vyshnevyy, A.V. Arsenin, V.S. Volkov, K.S. Novoselov, Exploring van der Waals materials with high anisotropy: geometrical and optical approaches, Light Sci Appl 13 (2024) 68.
[10] X. Li, L. Yao, W. Tao, J. Zhao, H. Zhu, Ultrafast intrinsic excited state localization m 2D layered As2S3 by interlayer bond formation, Chin. J. Chem. Phys. 36 (2023) 646–654.
[11] X.-M. Wang, L. Chen, E. Sowade, R.D. Rodriguez, E. Sheremet, C.-M. Yu, R. R. Baumann, J.-J. Chen, Ultra-uniform and Very Thin Ag nanowires synthesized via the synergy of Cl, Br and Fe for transparent conductive films, Nanomaterials (Basel) 10 (2020), https://doi.org/10.3390/nano10020237.
[12] N. Miao, J. Zhou, B. Sa, B. Xu, Z. Sun, Few-layer arsenic trichalcogenides: emerging two-dimensional semiconductors with tunable indirect-direct band-gaps, J. Alloys Compd. 699 (2017) 554–560.
[13] G.V. Gibbs, A.F. Wallace, R. Zallen, R.T. Downs, N.L. Ross, D.F. Cox, K.M. Rosso, Bond paths and van der Waals interactions in orpiment, As2S3, J. Phys. Chem. A 114 (2010) 6550–6557.
[14] W. Gao, J.R. Chelikowsky, Prediction of intrinsic ferroelectricity and large piezoelectricity in monolayer arsenic chalcogenides, Nano Lett 20 (2020) 8346–8352.
[15] H. Kaur, B. Konkena, M. McCrystall, K. Synnatschke, C. Gabbett, J. Munuera, R. Smith, Y. Jiang, R. Bekarevich, L. Jones, V. Nicolosi, J.N. Coleman, Liquid-phase exfoliation of arsenic Trisulfide (AsS) nanosheets and their use as anodes in potassium-ion batteries, ACS Nano 18 (2024) 20213–20225.
[16] Y. Zhang, M. Liao, J. Guo, N. Xu, X. Xie, Q. Fan, The co-transport of Cd(II) with nanoscale AsS in soil-packed column: effects of ionic strength, Chemosphere 286 (2022) 131628.
[17] M. Šiškins, M. Lee, F. Alijani, M.R. van Blankenstein, D. Davidovikj, H.S.J. van der Zant, P.G. Steeneken, Highly anisotropic mechanical and optical properties of 2D layered AsS membranes, ACS Nano 13 (2019) 10845–10851.
[18] D.J.E. Mullen, W. Nowacki, Refinement of the crystal structures of realgar, AsS and orpiment, As2S3, Z. Krist. 136 (1972) 48–65.
[19] T. Bu, H. Gao, Y. Yao, J. Wang, A.J. Pollard, E.J. Legge, C.A. Clifford, A. Delvallée, S. Ducourtieux, M.A. Lawn, B. Babic, V.A. Coleman, Å. Jämting, S. Zou, M. Chen, Z. J. Jakubek, E. Iacob, N. Chanthawong, K. Mongkolsuttirat, G. Zeng, C.M. Almeida,

B.-C. He, L. Hyde, L. Ren, Thickness measurements of graphene oxide flakes using atomic force microscopy: results of an international interlaboratory comparison, Nanotechnology 34 (2023), https://doi.org/10.1088/1361-6528/acbf58.
[20] C.J. Shearer, A.D. Slattery, A.J. Stapleton, J.G. Shapter, C.T. Gibson, Accurate thickness measurement of graphene, Nanotechnology 27 (2016) 125704.
[21] H. Cheng, Y. Zhou, R.L. Frost, Structure comparison of Orpiment and Realgar by Raman spectroscopy, Spectrosc. Lett. 50 (2017) 23–29.
[22] T.-H. Tran, R.D. Rodriguez, D. Cheshev, N.E. Villa, M. Awais Aslam, J. Pešić, A. Matković, E. Sheremet, A universal substrate for the nanoscale investigation of two-dimensional materials, Appl. Surf. Sci. 604 (2022) 154585.
[23] Z. Chen, T. Ma, W. Wei, W.-Y. Wong, C. Zhao, B.-J. Ni, Work function-guided electrocatalyst design, Adv. Mater. 36 (2024) e2401568.
[24] P.A. Fernández Garrillo, B. Grévin, N. Chevalier, Ł. Borowik, Calibrated work function mapping by Kelvin probe force microscopy, Rev. Sci. Instrum. 89 (2018) 043702.
[25] Y. Lv, J. Cui, Z.M. Jiang, X. Yang, Nanoscale electrical property studies of individual GeSi quantum rings by conductive scanning probe microscopy, Nanoscale Res. Lett. 7 (2012) 659.
[26] R. Zallen, D.F. Blossey, The optical properties, electronic structure, and photoconductivity of arsenic chalcogenide layer crystals. Optical and Electrical Properties, Springer, Netherlands, Dordrecht, 1976, pp. 231–272.
[27] E.V. Rut'kov, E.Y. Afanas'eva, N.R. Gall, Graphene and graphite work function depending on layer number on *Re*, Diam. Relat. Mater. 101 (2020) 107576.
[28] T.A. Khachaturova, V.G. But'ko, A.A. Gusev, Electronic structure and properties of two-dimensional silicon dioxide, JETP Lett 115 (2022) 41–44.
[29] Z. Zhang, J.T. Yates Jr, Band bending in semiconductors: chemical and physical consequences at surfaces and interfaces, Chem. Rev. 112 (2012) 5520–5551.
[30] A.P. Herman, S.J. Zelewski, K. Misztal, R. Kudrawiec, Probing the long-lived photo-generated charge carriers in transition metal dichalcogenides by time-resolved microwave photoconductivity, Nanophotonics 11 (2022) 1335–1344.
[31] F. Banhart, J. Kotakoski, A.V. Krasheninnikov, Structural defects in graphene, ACS Nano 5 (2011) 26–41.
[32] J. Jiang, T. Xu, J. Lu, L. Sun, Z. Ni, Defect engineering in 2D materials: precise manipulation and improved functionalities, Research 2019 (2019) 4641739.
[33] J. Jiang, C. Ling, T. Xu, W. Wang, X. Niu, A. Zafar, Z. Yan, X. Wang, Y. You, L. Sun, J. Lu, J. Wang, Z. Ni, Defect engineering for modulating the trap states in 2D photoconductors, Adv. Mater. (2018) e1804332.
[34] S. Ismail-Beigi, S.G. Louie, Self-trapped excitons in silicon dioxide: mechanism and properties, Phys. Rev. Lett. 95 (2005) 156401.
[35] Q. Ding, Y. Shi, M. Chen, H. Li, X. Yang, Y. Qu, W. Liang, M. Sun, Ultrafast Dynamics of Plasmon-Exciton Interaction of Ag nanowire- graphene hybrids for surface catalytic reactions, Sci. Rep. 6 (2016) 32724.
[36] R.P.N. Tripathi, X. Yang, J. Gao, Anisotropic third-harmonic generation of exfoliated AsS thin flakes, Opt. Express 30 (2022) 22661–22670.
[37] X. Ren, E. Tan, X. Lang, T. You, L. Jiang, H. Zhang, P. Yin, L. Guo, Observing reduction of 4-nitrobenzenthiol on gold nanoparticles in situ using surface-enhanced Raman spectroscopy, Phys. Chem. Chem. Phys. 15 (2013) 14196–14201.
[38] Y. Fang, Y. Li, H. Xu, M. Sun, Ascertaining p,p'-dimercaptoazobenzene produced from p-aminothiophenol by selective catalytic coupling reaction on silver nanoparticles, Langmuir 26 (2010) 7737–7746.